Physical Origin of Threshold Switching in Amorphous Chromium-Doped V$_2$O$_3$

Johannes Mohr,* Christopher Bengel, Tyler Hennen, Daniel Bedau, Stephan Menzel, Rainer Waser, and Dirk J. Wouters

Devices made of amorphous thin films of the prototypical Mott-insulator chromium-doped V$_2$O$_3$ show a threshold and negative differential resistance effect after an electroforming step. Here, it is demonstrated that this effect is caused by the formation of a crystalline filament, in which a thermal runaway effect can occur. A compact model is developed that can describe the switching behavior as well as its inherent variability. The influence of the doping concentration and oxygen stoichiometry on the switching behavior is characterized and by fitting the model to the experimental data, the underlying physical changes are extracted.

1. Introduction

In recent times, a variety of threshold switching devices have been investigated for use as selector devices for resistive crossbar memories,[1,2] nanoscale oscillators for reservoir computing,[3] and for neuromorphic applications.[4,5] Different physical mechanisms can be the origin of the threshold switching effect. Apart from ovonic threshold switching[6] and electrochemical mechanisms,[7] a large class is based on thermal effects. Some materials exhibiting a thermally driven phase transition, such as VO$_2$[8–10] or NbO$_x$,[4] are under consideration, but these suffer from a transition temperature that is either too low or too high for practical applications. In NbO$_x$, additionally, another distinct switching mode has been observed that is believed to be due to a thermal runaway effect.[11–13] Recently, this has also been observed in highly Cr-doped V$_2$O$_3$ (Cr:V$_2$O$_3$)-based nanoscale devices, which have a high switching speed and endurance, as well as a very stable threshold voltage.[14–16] This thermal runaway results from a region of S-type negative differential resistance (NDR) in the steady-state current–voltage characteristic of the device.

Practical applications will require integrating devices with complementary metal-oxide-semiconductor (CMOS)-based components, which puts limits on backend processing temperatures. However, in reported Cr:V$_2$O$_3$ devices, crystalline films were deposited with a high-temperature physical vapor deposition (PVD) process or a low-temperature deposition and a subsequent furnace anneal were used.[15,17] Ideally, devices should be fabricated from amorphous V$_2$O$_3$ deposited at room temperature. Both volatile and persistent switching effects have been reported for such films, but little is known about their physical origin, and how the switching is influenced by material properties such as doping concentration and oxygen stoichiometry.[14,17] This must be elucidated to enable fabrication of devices with optimized behavior. Furthermore, the reported switching mechanisms require a preceding electroforming step,[14] which is not needed for crystalline devices.[15] Therefore it should be clarified if this step is essential or can be avoided.

Here, we present results on amorphous Cr:V$_2$O$_3$ for different doping concentrations, oxygen stoichiometries, and thicknesses. First, it is demonstrated that a forming step is necessary to crystallize a filament in the material. We then show results that indicate that the switching mechanism in the filament is the same as in cells consisting fully of crystalline oxide, by describing the observations with a thermal feedback model. The model additionally considers the variability introduced by the different configurations of the crystallized domains. Finally, we investigate how the switching behavior changes for different material compositions.

2. Experimental Section

The devices investigated in this work were line arrays consisting of 32 individual cells arranged in a row (**Figure 1**a,b). These were fabricated on Si substrates with a $\approx$400 nm-thick layer of thermal SiO$_2$. First, a 30 nm-thick Pt bottom electrode was deposited by DC sputtering with a 5 nm Ti adhesion layer. A 30 nm SiO$_2$ layer

J. Mohr, C. Bengel, T. Hennen, R. Waser, D. J. Wouters
Institute of Materials in Electrical Engineering and Information Technology II
RWTH Aachen University
52074 Aachen, Germany
E-mail: mohr@iwe.rwth-aachen.de

D. Bedau
Western Digital San Jose Research Center
5601 Great Oaks Parkway, San Jose, CA 95119, USA

S. Menzel, R. Waser
Peter Grünberg Institute PGI 7
Research Center Jülich
52428 Jülich, Germany

The ORCID identification number(s) for the author(s) of this article can be found under https://doi.org/10.1002/pssa.202300405.

ADVANCED
SCIENCE NEWS
www.advancedsciencenews.com

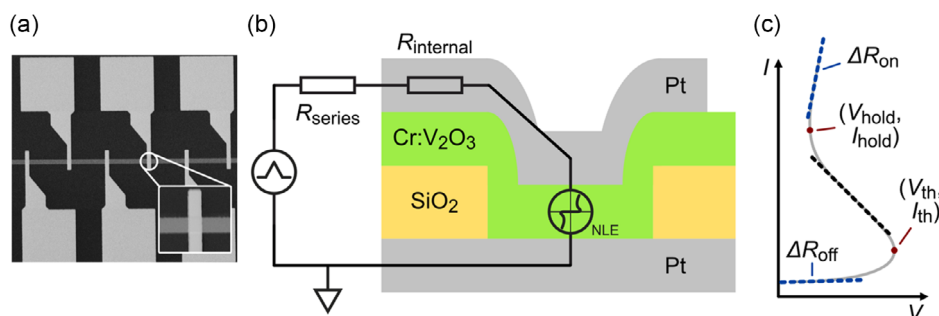physica
pss status
solidi a
www.pss-a.com

Figure 1. a) Scanning electron microscopy image of a row of devices. The horizontal line is the trench in the SiO_2 layer, the vertical structures are the Pt top electrodes connected to contact pads. The bottom electrode contact is not shown. b) Cross section of a cell. The active device area is defined by the trench and the top electrode (indicated as nonlinear element (NLE)). The overlaid circuit diagram gives the electrical connections during the measurements. In addition to the intentionally applied series resistor (R_{series}), an internal resistance of the electrodes is considered ($R_{internal}$). c) Sketch of a typical measured curve. The region with S-type NDR is indicated by the black (dashed) line in the center. The two points delimiting this region, extracted for the analysis, are marked by red dots. Blue lines indicate the regions where the on and off resistances were extracted.

was then deposited by electron beam evaporation. Trenches of different widths (3, 5, 7, 10 µm) were etched into this after a standard photolithography step. Then, a full film of Cr-doped V_2O_3, either 30 or 100 nm thick, was deposited by reactive radio frequency (RF) sputtering from a V/Cr alloy target. Two different targets with either 5 or 15% Cr alloyed into V were used (3N purity). An oxygen/argon mixture was introduced during this to form V_2O_3. To achieve the correct composition, very low oxygen contents of 0.06 and 0.14% were required. This was achieved utilizing two gas sources, a 1% O_2 in Ar mixture and a pure Ar source (both 5N purity). For brevity, we referred to the former as the O_2 flow in the remainder of this work. By combining them in a ratio of 6 sccm/94 sccm or 14 sccm/86 sccm, the desired low oxygen concentration was realized. The pressure in the chamber was controlled by an outflow valve to be 0.01 mbar. Because sputtering is a nonequilibrium technique, this allows forming reduced phases compared to the fully oxidized V_2O_5.[17] The composition was verified in a previous work by X-ray photoelectron spectroscopy (XPS), where +3 and +4 oxidation states were found for vanadium, indicating a slightly oxygen-rich V_2O_3, and a good transfer of the Cr doping concentrations to the films was confirmed.[14,17] A direct characterization by X-ray method was not possible due to the amorphous nature of the films; however, if a crystalline film was fabricated with the same settings and heated deposition, V_2O_3 was obtained.[17] Finally, 30 nm-thick Pt top electrodes were fabricated by a lift-off step. Their width was the same as the corresponding trench's, resulting in square devices (see inset in Figure 1a).

Eight different device stacks were considered (**Table 1**), consisting of any combination of two chromium concentrations (5 and 15%), two oxygen flows during deposition (6 and 14 sccm), and the thicknesses 30 and 100 nm.

For experimental characterization, the 32 top electrodes were contacted with a probe card connected to a custom array measurement system manufactured by aixACCT Systems. The common bottom electrode was grounded with a single probe. The four voltage output channels of the system were set up so that resistors of 500 Ω, 1000 Ω, and 3000 Ω could be placed in series with the cells during the measurements (R_{series}), and the last channel allowed a direct connection.

Table 1. Investigated $Cr:V_2O_3$ layers.

Sample	Cr [%]	O_2 [sccm]	Thickness [nm]
1	15	6	30
2	15	14	30
3	15	6	100
4	15	14	100
5	5	6	30
6	5	14	30
7	5	6	100
8	5	14	100

The series resistors introduced negative current–voltage feedback to the system and were used for two related reasons. The first was to enable a stable characterization of NDR steady-state curves, which can be separated by runaway transitions between two stable branches if the series resistance is not sufficiently large.[18] The second reason for the series resistance was to prevent destruction of the device in the event of runaway switching by limiting the exposure of the device to voltage and current. If the device conductance switches with high speed relative to the applied voltage sweep rate, a transition along the negatively sloped load line will be recorded before stabilizing at reduced device voltage. This phenomenon has been called "snapback," independently of the mechanism driving the switching process.[19–22] However, using a large enough series resistance, the switching can be controlled in a more continuous way, and characteristic NDR curves can be observed in the measurement.[23]

The series resistance value is a compromise between the desired large output impedance and the maximum available voltage from the source. Due to the voltage divider effect, if the resistor is too large, the voltage that reaches the device electrodes may not be large enough to induce switching. For the analysis and in the figures below, the voltage across the device electrodes was calculated by subtracting the voltage drop over the series resistor from the applied voltage.

The measurements were performed by applying voltage sweeps with different peak voltages (2–8 V, in 2 V steps) and

series resistors. The sweep duration was fixed to 10 ms, resulting in sweep rates of 0.2–0.8 V ms^{-1}. The combinations were selected at random for each measurement, to prevent any drifts from influencing the results. Ten combinations were tested for each cell, with 64 cells characterized for each trench width. As four widths were available, this yielded 2560 measurements for each of the layers in Table 1. Before and after each sweep, the resistance of the cell was measured using 0.1 V pulses.

For the analysis the data were first cleaned, by removing defective cells exhibiting a short or open circuit due to contact issues. Then, from each individual sweep, characteristic data were extracted (indicated in Figure 1c), such as the voltage and current at the onset of NDR (V_{th}, I_{th}) and at the point where differential resistance turned positive again (V_{hold}, I_{hold}). The width of the NDR region, defined as $V_{th}-V_{hold}$, was referred to as ΔV_{NDR}. Additionally, leakage resistance (ΔR_{off}) and the on resistance (ΔR_{on}) were approximated by fitting lines to the lowest and highest current section of the curve, respectively. Naturally, it is not guaranteed that a cell exhibits NDR behavior, and all points exist. Where this was not the case the datum was marked accordingly. For the analysis of the variability and material dependence, some outliers were removed to prevent distortion of the averages.

The forming event was detected by evaluating the ratio of resistances before and after each sweep. The first sweep where the resistance was reduced by more than half was considered the forming, and all sweeps before this were marked as pretransition, while those after were considered postforming.

Temperature-dependent measurements were done on individual cells using a Keithley 2636B source-measure unit between 30 and 80 °C.

3. Simulation Model

To describe the experimental results, a simple model was used that describes the electronic conduction and accounts for the self-heating of the device at higher currents. This model is closely related to other models for volatile threshold switching devices.[16,24] An equivalent circuit diagram is shown in **Figure 2**.

The electron conduction is described by

$$I(V_{device}, T) = a \times V_{device} \times \exp\left(-\frac{b}{k_B T}\right) \times \exp(c\sqrt{V_{device}}) \quad (1)$$

where a is a scaling factor for the current, b describes the energy barrier for the electronic conduction, and c represents the scaling of the voltage dependence of the current.[15,16] T is the device temperature, increased above the ambient temperature due to
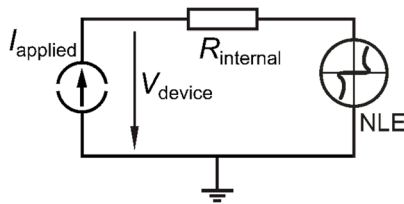
the self-heating of the device. Newton's law of cooling describes this self-heating as

$$C_{th}\frac{dT}{dt} = I \times V_{device} - \frac{T - T_0}{R_{th}} \quad (2)$$

where C_{th} and R_{th} denote the thermal capacitance and thermal resistance, respectively. T_0 is the ambient temperature, which is chosen as 293 K for all simulations if not denoted otherwise. The input current is applied as repeated triangle sweeps with a rise time of 10 ms from 0 to 10 mA and a fall time of 10 ms from 10 to 0 mA.

The model is then expanded to account for device-to-device (d2d) and cycle-to-cycle (c2c) variability in a manner closely related to the approach in a previous work.[25] For this purpose, all parameters of the compact model are assigned a mean value as well as a global maximum and minimum value. d2d variability is introduced by drawing the initial parameters for each device from a Gaussian distribution, which is described by each parameters' mean value and the coefficient of variation (var$K$). These distributions are truncated by the global maximum and minimum values for each parameter. c2c variability is achieved by adapting the parameter values of the compact model over time. The maximum variation around the initial parameter value of each device is determined by the parameter c2c percentage (c2c%). For the c2c variability, the parameters are changed after each triangular pulse. The maximum change of each parameter between two cycles is given by the maximum stepsize (maxstep). The change of a parameter x from step (k–1) to step k can then be described by

$$x_k = x_{k-1} \times (1 \pm P \times \text{maxstep}) \quad (3)$$

where P is a random number between zero and one scaling the applied step size. The direction of the change of the parameter value is randomly assigned between '+' and '−' with a 50% chance for each direction. If the value calculated from Equation (3) exceeds the limitations given by c2c%, the value is clipped to the corresponding parameter limit.

The adapted parameter values and their limits are shown in **Table 2** for the 100 nm-thick sample with 5% Cr doping and 14 sccm O_2, corresponding to the measurements in Section 4.

Table 2. Parameters of the compact model.

Symbol	Minimum	Median	Maximum
a [S]	4.2	6	7.2
b [eV]	0.144	0.18	0.216
c [V$^{-1/2}$]	1.05	1.5	1.8
$R_{internal}$ [Ω]	140	200	260
C_{th} [J K^{-1}]	0.7×10^{-11}	1×10^{-11}	1.2×10^{-11}
R_{th} [K W^{-1}]	0.7×10^6	1×10^6	1.2×10^6
var$K$	–	0.3	–
c2c%	–	5%	–
maximum step size	–	3%	–

Figure 2. The circuit diagram used to simulate the compact model and to adapt its parameters to the measurements.

4. Origin of NDR

4.1. Forming

The electrical characterization reveals that an NDR effect can be realized in all eight investigated stacks, however with different curve shapes and reliabilities. In most cases, a forming step is necessary. A typical example is shown in **Figure 3**a. Initially, the cells exhibit a relatively high resistance. When a sufficiently high-voltage sweep is applied, first the device current rises gradually and then a sudden increase in the conductivity is observed. Because a resistor is applied in series with the cell to limit the current, this is accompanied by a reduction in the cell voltage due to the voltage divider effect. When the voltage is reduced again, the current will remain at much higher values than during the first half of the cycle, indicating a permanent change in the resistance of the cell. In subsequent cycles, the I–V characteristic shows a negative resistance behavior at much lower voltages (under 1 V). This does not result in permanent changes and can be repeated multiple times with identical behavior. Ideally, a smooth curve is observed; however, the measurement can also show a discontinuous jump with a small hysteresis if the series resistor is too small.[18]

Figure 3b demonstrates the necessity of the forming step to reliably obtain NDR behavior. For all samples, it compares the number of devices in which NDR was observed before and after a forming event had occurred. Only in a negligible number of cells it is found without forming, whereas afterwards it is often seen. Clearly, the number of successful forming events is different between the two film thicknesses. Thinner films appear to be more difficult to form. Additionally, higher forming voltages are observed for higher doping concentrations.

This is a good indication regarding the mechanism of the forming event. It has been suspected that it is due to local crystallization of the amorphous oxide due to Joule heating.[14,17] As the higher doped films are more insulating (experimental results in other studies,[17,26] detailed theoretical discussion of the electronic structure by Grieger et al.[27]), a larger voltage will be necessary to achieve the required temperatures.

The conductivity in the amorphous oxide shows a strong dependence on temperature (see Figure S1, Supporting Information), which might play a role in the forming process. When a sufficient voltage is applied to the cell, Joule heating will increase its internal temperature. This will reduce its resistance and therefore lead to even more current flowing. This raises the temperature even more, leading to a feedback loop until a temperature is reached that is high enough for the material to crystallize.

Due to this runaway nature, it can be expected that a thermal constriction will occur, with only a small filamentary path through the oxide heating up strongly. This effect has been shown to be significant for other materials.[28] As this will occur preferentially at defects such as grain boundaries, the crystallized domains will also form filaments.

This is indeed observed experimentally: Figure 3c shows some characteristic switching properties over the cell size. Essentially, no scaling with the width is seen, clear evidence for the filamentary nature of the forming process. A slight exception is the (differential) resistivity in the on state which decreases somewhat for larger cells. This is likely dominated by the lead resistance of the electrodes, which will be lower if they are wider. Because the influence of the cell size is largely negligible, in the following analysis, all sizes are considered together.

Additionally, no significant influence of the series resistor used during the forming cycle was found. It would be expected
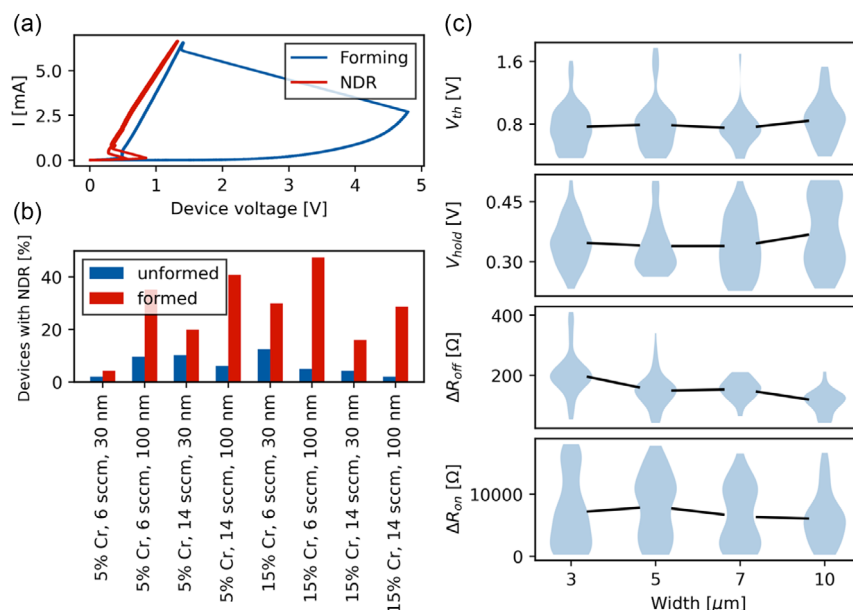

Figure 3. a) A typical forming loop and a subsequent NDR curve, measured on the 100 nm, 5% Cr, 6 sccm sample. b) The percentage of devices that show NDR behavior in the unformed and formed states for the different materials. c) Distribution of the switching parameters as a function of the device width for the same sample as in (a).

that a higher value would limit the current to lower values and a smaller filament would be found. The reason this is not observed is likely due to the capacitance of the cell itself and of the leads connecting to it. This capacitance is located closer to the cell than the current limiting resistor and discharges through the cell on the onset of forming. This reduces the limiting effect.

The surprising observation that the thinner films are more difficult to form, even though the electric fields should be higher, is believed to be due to the lower maximum temperature in the cell. Because of the high thermal conductivity of the Pt electrodes, and especially the large bottom electrode, these will transfer the main part of the generated heat away from the cell. For the thick oxide, the center of the cell is separated by a thicker layer of relatively low-thermal conductivity oxide from these and will reach a higher temperature. The thinner cells are more effectively cooled, and therefore it is less likely that the necessary temperature for crystallization is reached.

Figure 3b also shows some occurrence of NDR in devices without forming. We attribute this mainly to the presence of defects in the material, which in many transition metal oxides are mobile under the influence of an electric field.[29] In this case, the material might be slightly oxygen rich, either due to deposition or exposure to ambient atmosphere. The defects mobility is significantly enhanced by elevated temperatures due to Joule heating, which can lead to well-known nonvolatile switching effects.[30] In these cases, the SET transition can appear as an NDR region.[18,21] Here, a more moderate drift effect that does not result in switching might be active. The influence of excess oxygen in $Cr:V_2O_3$ is approximately opposite to chromium doping and can compensate its effect.[31] If there is a drift of oxygen, it will have a proportionally bigger influence on the 5%-doped films, because less uncompensated Cr remains. This is indeed observed, the ratio of unformed to formed devices with NDR is clearly larger for the lower doped samples (comparing identical thicknesses and O_2 flows). Further evidence is that this ratio also appears to be larger for thinner devices, where a stronger electric field can be expected to lead to an increased drift of defects.

The fact that this unformed NDR effect occurs only occasionally indicates that it is enabled by imperfections in the film, such as boundaries between the growth columns, and would not be found in industrial quality films. Because of this, we only consider the formed devices in the remainder of this work.

4.2. NDR

After forming, the devices show an S-type NDR behavior with typical threshold voltages of 0.5–1 V at room temperature. The off resistance at voltages below the threshold is on the order of a few kiloohm, the on resistance is about 100–200 Ω. The precise values differ between materials, as will be discussed below, as well as between different devices on one sample. As the proposed explanation for the switching is based on a self-heating effect, it should have a clear dependence on the ambient temperature. **Figure 4**a shows measurement results up to 80 °C with a 10 kΩ series resistor. At room temperature, NDR is clearly seen, but the curve has several kinks. This is believed to be due to a filament that consists of multiple crystalline grains, which might have an onset of NDR at slightly different voltages, for example, due to their different sizes. With increasing ambient temperature, the onset of the NDR is shifted toward lower voltages, and the width of the NDR region (ΔV_{NDR}) is reduced. Additionally, the leakage current at low voltages increases significantly with temperature. This continues, until the NDR disappears completely at the highest temperatures. It should be noted that this not a permanent change to the device; if the ambient temperature is reduced again, the NDR is recovered. This trend is reproduced by the model as discussed below; qualitatively, it can be understood as a consequence of the strong thermal activation of the conductivity. The internal device temperature, and therefore onset of NDR, is determined by the dissipated power. An elevated ambient temperature increases the current for a fixed voltage; consequently, to dissipate the same power, a lower voltage is needed. This leads to a reduction of V_{th}, whereas the behavior at high currents is mainly limited by the (constant) internal series resistance. Therefore, the NDR window is reduced, and due to the higher conductivity at low voltages the transition to the low on-resistances is smoothed out.

Some of the curves show a slight hysteresis between the increasing and decreasing part of the voltage sweep. This might in part be due to the thermal capacitance of the device, which
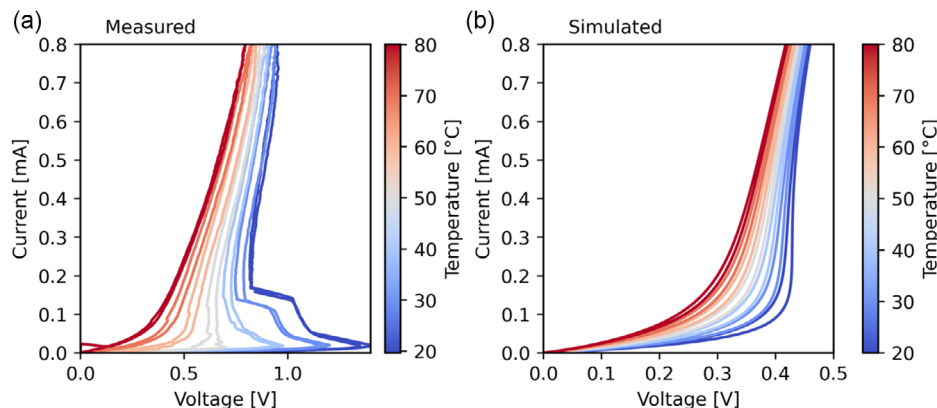

Figure 4. a) Measured switching curves for different temperatures for the 5% Cr, 6 sccm O_2 sample. b) Corresponding simulation using the parameters given in Table 1.

would lead to a higher temperature during the falling part of the sweep; however, another significant influence might be again due to defects mobile under the influence of the electric field, that might lead to a gradual drift in cell behavior.

Relatively high currents of nearly 1 mA are observed in the experiments. This likely has two reasons. First, even though Cr:V$_2$O$_3$ is many orders of magnitude more insulating than metallic, undoped V$_2$O$_3$, it is still relatively conductive ($\approx$1–10 Ω cm[32]) compared to other insulators. The second reason for the high currents above the NDR region is likely the strong increase in conductivity due to self-heating. It should be noted that a low resistance in this region is desirable for device applications, and the current at the onset of the NDR is much lower (<100 μA).

The simulation results in Figure 4b match the observed behavior qualitatively quite well, indicating that the thermal runaway model is adequate and the conduction mechanism can be described for both ambient and elevated temperatures by Equation (1). As the simulations consider a homogeneous device, the curves are smooth. The hysteresis here is only due to thermal capacitance and is smaller than the experimentally observed one, indicating that at least some drift is present. Quantitatively, there is some disagreement between the simulated and experimental values for the threshold voltage. This is because the model is adapted to an average device, whereas the physical cells show significant variability. This highlights the importance of collecting many loops to allow for valid conclusions.

It should be noted that the model explains the observations purely by modeling a thermal runaway, without assuming that any Mott metal–insulator transition (MIT) occurs. While in principle, thermal runaway and MIT can be found in the same device.[13] This is unlikely here, because the doping concentrations used are most likely too high and therefore the films too far from the phase boundary.[32] A field-triggered MIT might be expected for about 2% doping, but these films have too low resistance for practical applications.

4.3. Variability

The total variability can be decomposed into two parts, the variability between different measurement cycles in a single device and between different cells on a sample. Because the NDR behavior was most prevalent in the thicker films, these offer the largest available datasets. Therefore, only they were considered in the evaluation of the variability. **Figure 5**a shows the distribution of the threshold voltage as a representative parameter for different materials. The c2c variability is defined as the largest deviation from the mean value measured for all cycles in one cell; the d2d variability is the (absolute) difference between the mean in one cell and the mean over the whole sample. Clearly, in all samples, the variation between devices is much larger than between cycles. The former is $\approx$0.3 V while the latter is typically significantly less than 0.1 V. Interestingly, there are some differences between materials. The c2c variability seems to have outliers at much higher values than typical for the 5% Cr-doped samples. This might be related to the hysteresis seen in the I–V loops and is suspected to be due to a drift of crystallographic defects under the influence of the field, potentially accelerated by the elevated device temperature during switching.[30] This could
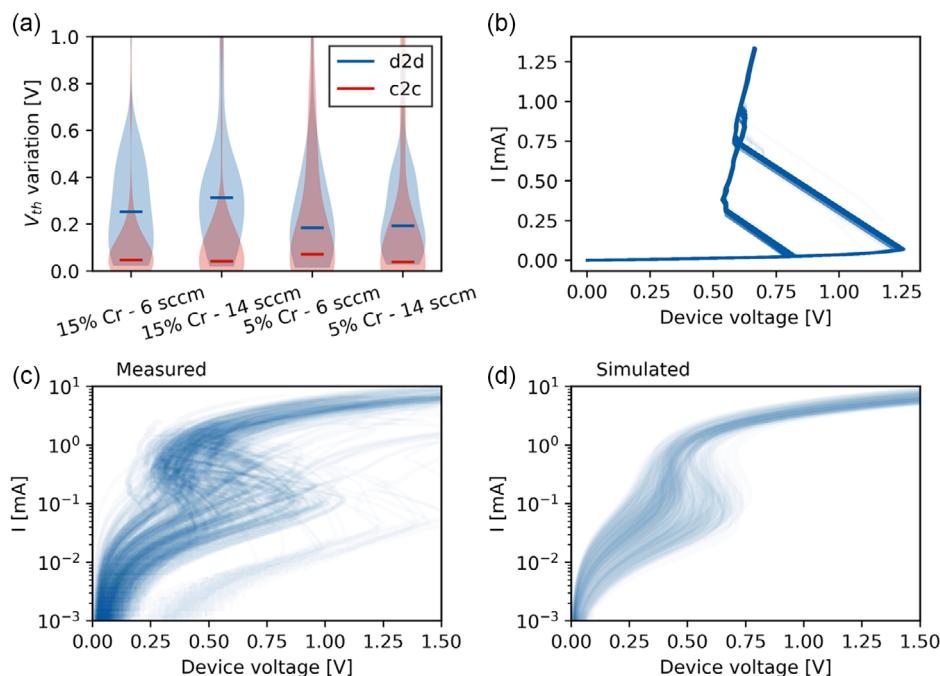

Figure 5. a) Variability of the threshold voltage between cycles and devices for different materials. The lines indicate the median values. b) 1000 consecutive cycles measured with a 1 kΩ series resistor on a single device. All loops are nearly identical. Note that the individual loops are drawn with the same level of transparency as those in (c, d). c) Variability of the switching behavior for the 5% Cr, 6 sccm O$_2$ sample. The variation is much larger than in (b), because multiple devices are shown. d) Corresponding simulation results.

then lead to shifts in the threshold voltage. The precise nature of defects in the formed filament is not known with certainty. However, it has been speculated that higher chromium doping promotes the formation of the correct stoichiometry in V_2O_3, as chromium oxide only exists as Cr_2O_3, while for vanadium oxide many different compositions are known.[17] This could explain that less defects are present in the higher doped samples, and consequently less variability is observed.

The much larger variability between devices is likely due to the poorly controlled forming process resulting in different sizes of the filament. It appears like the d2d variability is slightly higher for the 15% doped samples. However, as will be shown, these samples also exhibit higher values of the threshold voltage, so a larger absolute variation is expected.

The low variation between loops in one device is a key characteristic property of the thermal runaway in crystalline V_2O_3, which clearly distinguishes the switching from other mechanisms such as nanoionic effects, which typically show significant variation between cycles.[33,34] Because of this, it was investigated in more detail. Figure 5b shows 1000 consecutive loops in the same device. Clearly, the loops are nearly identical with a variation in the threshold voltage of about 50 mV. This is a very strong indication that the switching mechanism in the formed cells is the same as in crystalline V_2O_3.

Because the variability is an important concern for the practical application of the devices, and to confirm that it can indeed describe the switching process well, it was implemented in the simulation model. In Figure 5c,d 315 experimentally measured loops are compared to 1000 simulated ones. This shows that when variability is considered, the models predictions are also quantitatively correct. For example, the average onset of NDR is at $\approx$0.5 V and 100 μA in both measurement and simulation. The leakage current at 0.1 V is also comparable at about 3 μA, as well as the slope at high voltages.

5. Influence of Material Composition

To be able to optimize the devices for applications, it is important to characterize how changes to the material composition affect switching. For this, we compare the median values of the switching parameters for different doping concentrations and oxygen stoichiometries. Again, only the 100 nm-thick films are considered. In **Figure 6**a, these are shown grouped by each factor. This allows easy identification of the influence of material factors on switching parameters. Only those parameters showing a significant difference between samples are shown.

Clearly, the influence of the doping concentration is much more significant than that of the oxygen flow. Increasing it from 5 to 15% leads to an increase in the threshold voltage from $\approx$0.7–0.8 V, as well as an increase in the hold voltage from 0.3 to 0.6 V. Because the latter change is larger, this results in a decrease of ΔV_{NDR} from about 0.35–0.2 V. The leakage resistance ΔR_{off} increases with doping concentration, the change in ΔR_{on} appears insignificant.

The influence of stoichiometry is less clear. It appears that an increase in O_2 flow leads to a slight increase in ΔR_{on}; however, this change is much larger for the lower doped samples. For other parameters, it even appears like the direction of the change depends on the doping, for example, the threshold voltage seems to increase with O_2 for low doping concentrations, whereas for high ones it decreases. Of course, this might be simply due to random variation in the experiment, but it should be noted that the same trend is also observed for the hold voltage.

To elucidate the physical origins of these changes, we created four variations of the simulation model with parameters adapted to fit the measured characteristics for the four samples. A good agreement could be achieved in all cases (Figure S2, Supporting Information). In Figure 6b, the model parameters that show
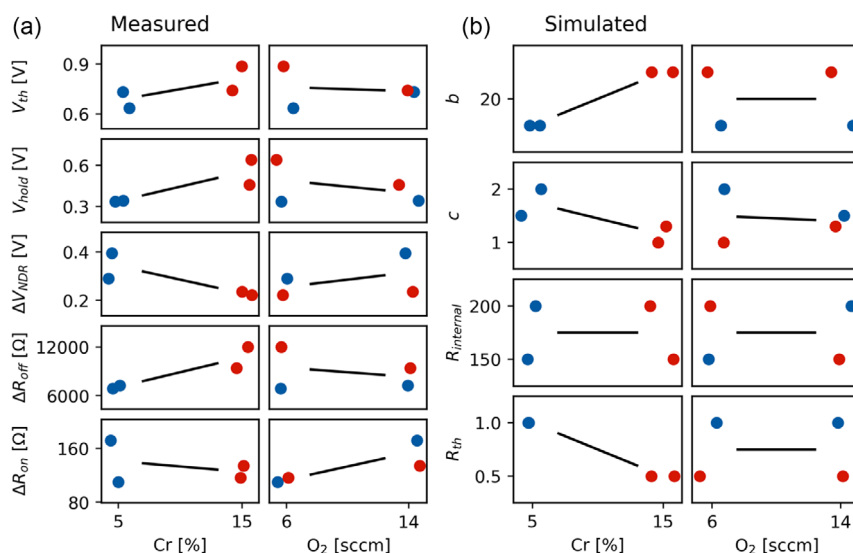

Figure 6. a) Switching parameters extracted from the measured data. Each dot corresponds to one of the 100 nm-thick samples and indicates the median value of a property. The same four dots, for example for V_{th}, are shown grouped by Cr and O_2. They are additionally colored by Cr, to highlight the different influences of O_2 dependent on doping. The solid lines connect the median values for each group. b) Parameters of the adapted simulation models.

significant changes are shown. The complete sets of parameters are given in Table S1, Supporting Information.

Clearly, b increases with doping concentration, while c decreases. The internal series resistance shows no influence, while the thermal resistance decreases. Matching the experimental results, the influence of O_2 is much more subtle. Only c and $R_{internal}$ might show an influence that is dependent on the doping concentration. c seems to increase with O_2 for high doping concentrations, while it decreases for low doping. $R_{internal}$ shows the opposite trend, but the changes are small and might be insignificant.

These results suggest the following preliminary understanding of the materials' influence. Most likely, as the addition of Cr to V_2O_3 opens a bandgap, in an effect that has been described as "chemical pressure" with 1% Cr corresponding to 4 kbar of pressure,[32,35] it is reasonable to assume that this bandgap widens with concentration (as the lattice parameters and resistivity change further after the MIT[26,32,36]). This is consistent with the observed increase in the energy barrier b. The higher doped material will then be less conductive for a given temperature,[17,26] explaining the increased leakage resistance. The switching voltages are higher, because at a given voltage the current is lower, and thus the cell temperature is as well.

The decrease in the thermal resistance is most likely not primarily due to a change in the thermal conductivity of the material, because any electronic contribution should decrease with the electrical conductivity, and the influence on the lattice is likely small due to the similar masses of V and Cr atoms (as has been observed for other doped oxides with A_2B_3 composition and semiconductors[37–39]). Probably this is due to a different size of the filament, which could result from different crystallization temperatures due to doping.

The decrease in c with Cr doping could be an effect due to the oxygen stoichiometry. If doping helps to stabilize the correct composition, as indicated by XPS measurements,[14,17] the number of defects in the material might be reduced, which could be contributing to conductivity.

6. Conclusion

The results of the present study indicate that the switching in amorphous $Cr:V_2O_3$ can be understood as a process in a filament crystallized during a forming step. The mechanism is very likely the same thermal runaway effect as in fully crystalline nanodevices, as it can be very well described by the same model and shares key properties such as the high stability of the threshold voltage or the decrease in the width of the NDR region with temperature. Therefore, in principle, a high-temperature deposition step can be avoided. The requirement for a forming step, however, leads to a significant variability between devices. Further work is needed to reduce this by improving the current compliance during forming. Potentially, an integrated series resistor close to the cell could aid in stabilizing the behavior.

Regarding the influence of the materials properties, chromium doping is clearly much more significant than oxygen stoichiometry. This is interesting, as the stoichiometry is believed to be very important in crystalline V_2O_3. A trade-off is found between the threshold voltage, which increases with

doping, and the leakage current, which is reduced. For practical applications, the devices must be integrated with other CMOS-based electronics. Because the operating voltages in modern CMOS nodes are very low (<1 V),[40] the 5 %-doped material should be chosen, due to the lower threshold voltage. This is especially true if they are used as selector devices in a ReRAM crossbar array, where an additional voltage drop over the memory cell must be considered. Doping concentrations significantly below 5% should be avoided due to excessive leakage currents.

Supporting Information

Supporting Information is available from the Wiley Online Library or from the author.

Conflict of Interest

The authors declare no conflict of interest.

Data Availability Statement

The data that support the findings of this study are available from the corresponding author upon reasonable request.

[1] E. Cha, J. Park, J. Woo, D. Lee, A. Prakash, H. Hwang, *Appl. Phys. Lett.* **2016**, *108*, 153502.

[2] K. Zhang, B. Wang, F. Wang, Y. Han, X. Jian, H. Zhang, H. S. Philip Wong, *IEEE Electron Device Lett.* **2016**, *37*, 978.

[3] W. Ma, T. Hennen, M. Lueker-Boden, R. Galbraith, J. Goode, W. H. Choi, P. Chiu, J. A. J. Rupp, D. J. Wouters, R. Waser, D. Bedau, *ISCAS2020* **2020**, *1*, 1.

[4] M. D. Pickett, G. Medeiros-Ribeiro, R. S. Williams, *Nat. Mater.* **2013**, *12*, 114.

[5] S. Kumar, J. P. Strachan, R. S. Williams, *Nature* **2017**, *548*, 318.

[6] S. R. Ovshinsky, *Phys. Rev. Lett.* **1968**, *21*, 1450.

[7] Z. Wang, M. Rao, R. Midya, S. Joshi, H. Jiang, P. Lin, W. Song, S. Asapu, Y. Zhuo, C. Li, H. Wu, Q. Xia, J. J. Yang, *Adv. Funct. Mater.* **2018**, *28*, 1704862.

[8] F. J. Morin, *Phys. Rev. Lett.* **1959**, *3*, 34.

[9] M. Son, J. Lee, J. Park, J. Shin, G. Choi, S. Jung, W. Lee, S. Kim, S. Park, H. Hwang, *IEEE Electron Device Lett.* **2011**, *32*, 1579.

[10] D. Li, A. A. Sharma, D. K. Gala, N. Shukla, H. Paik, S. Datta, D. G. Schlom, J. A. Bain, M. Skowronski, *ACS Appl. Mater. Interfaces* **2016**, *8*, 12908.

[11] C. Funck, S. Menzel, N. Aslam, H. Zhang, A. Hardtdegen, R. Waser, S. Hoffmann-Eifert, *Adv. Electron. Mater.* **2016**, *2*, 1600169.

[12] G. A. Gibson, S. Musunuru, J. Zhang, K. Vandenberghe, J. Lee, C. C. Hsieh, W. Jackson, Y. Jeon, D. Henze, Z. Li, R. Stanley Williams, *Appl. Phys. Lett.* **2016**, *108*, 023505.

[13] S. Kumar, Z. Wang, N. Davila, N. Kumari, K. J. Norris, X. Huang, J. P. Strachan, D. Vine, A. L. D. Kilcoyne, Y. Nishi, R. S. Williams, *Nat. Commun.* **2017**, *8*, 658.

[14] J. A. J. Rupp, M. Querré, A. Kindsmüller, M.-P. Besland, E. Janod, R. Dittmann, R. Waser, D. J. Wouters, *J. Appl. Phys.* **2018**, *123*, 44502.

[15] T. Hennen, D. Bedau, J. A. J. Rupp, C. Funck, S. Menzel, M. Grobis, R. Waser, D. J. Wouters, in *2018 IEEE Inter. Electron Devices Meeting (IEDM)*, Institute of Electrical and Electronics Engineers (IEEE), San Francisco, USA **2018**.

[16] T. Hennen, D. Bedau, J. A. J. Rupp, C. Funck, S. Menzel, M. Grobis, R. Waser, D. J. Wouters, in *2019 Ieee 11th Inter. Memory Workshop (imw 2019)*, IEEE, New York, NY, USA **2019**, p. 44.

[17] J. A. J. Rupp, Synthesis and Resistive Switching Mechanisms of Mott Insulators based on Undoped and Cr-doped Vanadium Oxide Thin Films.

[18] T. Hennen, E. Wichmann, R. Waser, D. J. Wouters, D. Bedau, *Rev. Sci. Instrum.* **2022**, *93*, 024705.

[19] X. Gao, T. J. Roskamp, T. Swoboda, C. M. M. Rosário, S. Smink, M. Muñoz Rojo, H. Hilgenkamp, *Adv. Electron. Mater.* **2023**, 2300304.

[20] A. A. Sharma, M. Noman, M. Abdelmoula, M. Skowronski, J. A. Bain, *Adv. Funct. Mater.* **2014**, *24*, 5522.

[21] A. Fantini, D. J. Wouters, R. Degraeve, L. Goux, L. Pantisano, G. Kar, Y.-Y. Chen, B. Govoreanu, J. A. Kittl, L. Altimime, M. Jurczak, in *2012 4th IEEE Inter. Memory Workshop*, IEEE, New York, NY, USA **2012**, pp. 1–4.

[22] D. J. Wouters, L. Zhang, A. Fantini, R. Degraeve, L. Goux, Y. Y. Chen, B. Govoreanu, G. S. Kar, G. V. Groeseneken, M. Jurczak, *IEEE Electron Device Lett.* **2012**, *33*, 1186.

[23] R. S. Mackay, *Am. J. Phys.* **1958**, *26*, 60.

[24] S. Slesazeck, H. Mähne, H. Wylezich, A. Wachowiak, J. Radhakrishnan, A. Ascoli, R. Tetzlaff, T. Mikolajick, *RSC Adv.* **2015**, *5*, 102318.

[25] C. Bengel, A. Siemon, F. Cüppers, S. Hoffmann-Eifert, A. Hardtdegen, M. Von Witzleben, L. Hellmich, R. Waser, S. Menzel, *IEEE Trans. Circuits Syst. I: Regul. Pap.* **2020**, *67*, 4618.

[26] P. Homm, L. Dillemans, M. Menghini, B. Van Bilzen, P. Bakalov, C. Y. Su, R. Lieten, M. Houssa, D. Nasr Esfahani, L. Covaci, F. M. Peeters, J. W. Seo, J. P. Locquet, *Appl. Phys. Lett.* **2015**, *107*, 149901.

[27] D. Grieger, F. Lechermann, *Phys. Rev. B: Condens. Matter Mater. Phys.* **2014**, *90*.

[28] J. M. Goodwill, A. A. Sharma, D. Li, J. A. Bain, M. Skowronski, *ACS Appl. Mater. Interfaces* **2017**, *9*, 11704.

[29] R. Dittmann, S. Menzel, R. Waser, *Adv. Phys.* **2021**, *70*, 155.

[30] S. Menzel, M. Waters, A. Marchewka, U. Böttger, R. Dittmann, R. Waser, *Adv. Funct. Mater.* **2011**, *21*, 4487.

[31] H. Kuwamoto, J. M. Honig, *J. Solid State Chem.* **1980**, *32*, 335.

[32] D. B. McWhan, J. P. Remeika, *Phys. Rev. B* **1970**, *2*, 3734.

[33] M. Lanza, R. Waser, D. Ielmini, J. J. Yang, L. Goux, J. Suñe, A. J. Kenyon, A. Mehonic, S. Spiga, V. Rana, S. Wiefels, S. Menzel, I. Valov, M. A. Villena, E. , X. Jing, F. Campabadal, M. B. Gonzalez, F. Aguirre, F. Palumbo, K. Zhu, J. B. Roldan, F. M. Puglisi, L. Larcher, T. H. Hou, T. Prodromakis, Y. Yang, P. Huang, T. Wan, Y. Chai, et al. *Standards for the Characterization of Endurance in Resistive Switching Devices*, Vol. 15, American Chemical Society, Washington, DC, USA **2021**, pp. 17214–17231.

[34] T. Hennen, A. Elias, J.-F. Nodin, G. Molas, R. Waser, D. J. Wouters, D. Bedau, *Front. Neurosci.* **2022**, *16*, 941753.

[35] D. B. McWhan, A. Menth, J. P. Remeika, W. F. Brinkman, T. M. Rice, *Phys. Rev. B* **1973**, *7*, 1920.

[36] T. Oyama, Y. Iimura, K. Takeuchi, T. Ishii, *J. Mater. Sci.* **1999**, *34*, 439.

[37] J. Sanghera, W. Kim, G. Villalobos, B. Shaw, C. Baker, J. Frantz, B. Sadowski, I. Aggarwal, *Materials* **2012**, *5*, 258.

[38] P. G. Klemens, *Phys. Rev.* **1960**, *119*, 507.

[39] K. R. Hahn, C. Melis, F. Bernardini, L. Colombo, *Front. Mech. Eng.* **2021**, *7*.

[40] S. Narasimha, B. Jagannathan, A. Ogino, D. Jaeger, B. Greene, C. Sheraw, K. Zhao, B. Haran, U. Kwon, A. K. M. Mahalingam, B. Kannan, B. Morganfeld, J. Dechene, C. Radens, A. Tessier, A. Hassan, H. Narisetty, I. Ahsan, M. Aminpur, C. An, M. Aquilino, A. Arya, R. Augur, N. Baliga, R. Bhelkar, G. Biery, A. Blauberg, N. Borjemscaia, A. Bryant, L. Cao, et al. in *2017 IEEE Inter. Electron Devices Meeting (IEDM)*, IEEE, New York, NY, USA **2017**, pp. 29.5.1–29.5.4.

2300405 (9 of 9)